

Pushing the boundaries
of chemistry?
It takes
#HumanChemistry

Make your curiosity and talent as a chemist matter to the world with a specialty chemicals leader. Together, we combine cutting-edge science with engineering expertise to create solutions that answer real-world problems. Find out how our approach to technology creates more opportunities for growth, and see what chemistry can do for you at:

evonik.com/career



Giant Thermal Transport Tuning at a Metal/Ferroelectric Interface

Yipeng Zang, Chen Di, Zhiming Geng, Xuejun Yan,* Dianxiang Ji, Ningchong Zheng, Xingyu Jiang, Hanyu Fu, Jianjun Wang, Wei Guo, Haoying Sun, Lu Han, Yunlei Zhou, Zhengbin Gu, Desheng Kong, Hugo Aramberri, Claudio Cazorla, Jorge Íñiguez, Riccardo Rurali, Longqing Chen, Jian Zhou, Di Wu, Minghui Lu,* Yuefeng Nie,* Yanfeng Chen, and Xiaoqing Pan

Interfacial thermal transport plays a prominent role in the thermal management of nanoscale objects and is of fundamental importance for basic research and nanodevices. At metal/insulator interfaces, a configuration commonly found in electronic devices, heat transport strongly depends upon the effective energy transfer from thermalized electrons in the metal to the phonons in the insulator. However, the mechanism of interfacial electron–phonon coupling and thermal transport at metal/insulator interfaces is not well understood. Here, the observation of a substantial enhancement of the interfacial thermal resistance and the important role of surface charges at the metal/ferroelectric interface in an Al/BiFeO₃ membrane are reported. By applying uniaxial strain, the interfacial thermal resistance can be varied substantially (up to an order of magnitude), which is attributed to the renormalized interfacial electron–phonon coupling caused by the charge redistribution at the interface due to the polarization rotation. These results imply that surface charges at a metal/insulator interface can substantially enhance the interfacial electron–phonon-mediated thermal coupling, providing a new route to optimize the thermal transport performance in next-generation nanodevices, power electronics, and thermal logic devices.

1. Introduction

The manipulation of heat flux through nanostructures and the dynamical tuning of the thermal properties of functional materials are critical issues in both basic research and electronic applications.^[1,2] High thermal conductivity materials, e.g., are desirable for electronic chips to promote heat dissipation and keep a low thermal budget,^[1b,3] while materials with as small as possible thermal conductivity can be used to achieve high thermoelectric figures of merit.^[4] As the miniaturization of electronic devices continues, fascinating thermal behavior may emerge, such as materials exhibiting negligible thermal resistance and phonons propagating ballistically.^[5] In the nanoscale realm, thermal resistance is dominated by the scattering of phonons at boundaries;^[6] hence, the conversion efficiency between

Y. Zang, C. Di, Z. Geng, X. Yan, D. Ji, N. Zheng, X. Jiang, H. Fu, W. Guo, H. Sun, L. Han, Y. Zhou, Z. Gu, D. Kong, J. Zhou, D. Wu, M. Lu, Y. Nie, Y. Chen
National Laboratory of Solid State Microstructures
Jiangsu Key Laboratory of Artificial Functional Materials
College of Engineering and Applied Science
Collaborative Innovation Center of Advanced Microstructures
Nanjing University
Nanjing 210093, China
E-mail: xjyan@nju.edu.cn; luminghui@nju.edu.cn; ynie@nju.edu.cn

J. Wang, L. Chen
Department of Materials Science and Engineering
Pennsylvania State University
State College, PA 16802, USA

H. Aramberri, J. Íñiguez
Materials Research and Technology Department
Luxembourg Institute of Science and Technology (LIST)
Avenue des Hauts-Fourneaux 5, Esch/Alzette L-4362, Luxembourg

 The ORCID identification number(s) for the author(s) of this article can be found under <https://doi.org/10.1002/adma.202105778>.

DOI: 10.1002/adma.202105778

C. Cazorla
Departament de Física
Universitat Politècnica de Catalunya
Campus Nord B4-B5, Barcelona E-08034, Spain

J. Íñiguez
Department of Physics and Materials Science
University of Luxembourg
41 Rue du Brill, Belvaux L-4422, Luxembourg

R. Rurali
Institut de Ciència de Materials de Barcelona
ICMAB-CSIC
Campus UAB
Bellaterra 08193, Spain

M. Lu
Department of Physics
Southern University of Science and Technology
Shenzhen 518055, China

X. Pan
Department of Materials Science and Engineering and Department of Physics and Astronomy
University of California, Irvine
916 Engineering Tower, Irvine, CA 92697, USA

heat energy carriers at the interfaces becomes very important.^[7] Since electrons and phonons dominate heat conduction in metals and insulators,^[5b,8] respectively, energy transfer must occur between them to allow heat transport across metal–insulator interfaces. Such electron (in metal)–phonon (in insulator) coupling can occur in either an indirect or direct manner.^[8] In the indirect case, electron–phonon coupling takes place on the metal side and a subsequent coupling between the phonons in the metal and in the insulator is required, just like in a junction between two insulators.^[9] In the direct case, the electron–phonon coupling occurs between the free electrons in the metal and the phonons in the insulator. However, the mechanisms underlying such interface electron–phonon couplings are not yet well understood, thus hindering the tuning of interface thermal conductance.

The design of materials with tailored thermal transport properties has received tremendous attention in recent years, with the result that many thermal conductivity engineering methods now are well established, including chemical element modification,^[10] superlattices,^[5a,5c] crystal structure optimization,^[11] and domain wall or grain boundary density control in ferroelectrics.^[12] Much recognition has been given to the tuning of interfacial thermal transport via chemical bonding modification,^[13] surface roughness engineering,^[14] or the insertion of buffer layers to promote interfacial heat fluxes.^[15] However, analogous investigations for metal/ferroelectric interfaces are rather limited despite their abundance in novel electronic

devices like thin-film nanocapacitors,^[16] nanoscale ferroelectric memories,^[16,17] and magnetic/ferroelectric tunnel junctions.^[18] Devising novel strategies to efficiently tune the interfacial thermal resistance of metal/ferroelectric interfaces, therefore, is pressing needed.

In this work, we synthesize freestanding ferroelectric BiFeO₃ (BFO) films and deposit an aluminum (Al) metal layer on top of them to fabricate metal/ferroelectric interfaces and thus explore their interfacial thermal transport properties under uniaxial strain. By time domain thermoreflectance (TDTR) measurements, we observe an extremely high tunability of the thermal transport across the Al/BFO interface that results from strain-driven rotation of the polarization in the ferroelectric BFO layer, which modifies the electron–phonon coupling at the metal/ferroelectric interface.

2. Results and Discussion

As shown in **Figure 1**, freestanding BFO films were synthesized by using SrTiO₃ (STO) as the substrate and water soluble Sr₃Al₂O₆ (SAO) as the sacrificial layer, as it has been previously reported.^[19] Freestanding BFO films were transferred onto a flexible substrate (poly(ethylene naphthalate) (PEN)) by using epoxy as the glue, and the flexible PEN substrate was mounted on a stretching stage to apply uniaxial strain.^[20] For thermal transport measurements, an aluminum layer was deposited

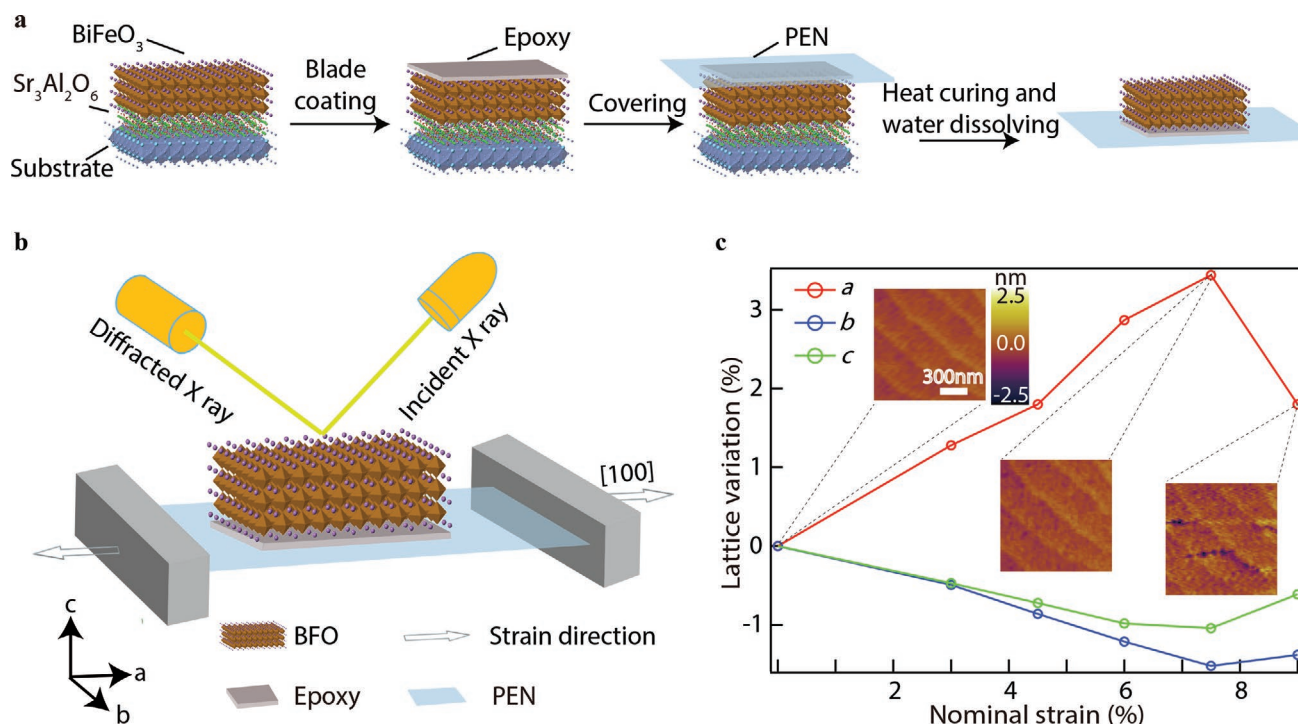


Figure 1. Synthesis and uniaxial strain engineering of freestanding BiFeO₃ (BFO) films. a) Schematic of the sample synthesis and transfer process of freestanding BiFeO₃ (BFO) films. The final BFO/epoxy/PEN structure is used for uniaxial strain experiments. b) Schematic of uniaxial stretching along the *a* axis. c) The lattice variation of transferred BFO films (5.2 nm) under different nominal strain showing the expansion of the lattice along the stretching direction and shrinkage along the other two axes. Nominal strain is defined as the percentage of the elongation of the PEN substrate. After reaching a maximum expansion of about 3.5%, the film forms microcracks and starts to relax. The inset topography images show a smooth step and terrace surface of the film and the formation of microcracks under large strain. Lattice strain is defined as $(L_x - L_0)/L_0$, where L_0 and L_x are the lattice constants under the nominal strain of 0% and $x\%$, respectively.

on the films to form an Al/BFO/epoxy/PEN heterostructure. Schematics of the sample transfer and uniaxial strain manipulation of the freestanding BFO films are shown in Figure 1a,b. The topography of the freestanding BFO films on PEN exhibits a high-quality surface showing clear atomic steps-and-terraces (Figure 1c and Figure S1b, Supporting Information).

In our experiments, we apply uniaxial strain along the high symmetry [100] pseudo-cubic direction to explore its impact on the thermal transport properties (Figure 1b). In principle, one expects that by applying uniaxial strain along [100], the lattice will expand along the stretched direction and shrink along the other two perpendicular dimensions, as indeed is experimentally confirmed by our in situ X-ray diffraction (XRD) measurements (Figure 1c). Uniaxial strain along the BFO [100] axis can be continuously increased up to around 3.5% (above this point the material starts to relieve stress by forming microcracks). Raw data of high-resolution XRD as a function of strain are provided in the Supporting Information (Figure S3, Supporting Information). The measured full-width at half-maximum does not show obvious changes under uniaxial strain (Figure S5, Supporting Information), indicating that no apparent domain migration or lattice slipping is taking place while applying strain.

The ferroelectric polarization of BFO films strongly relies on the lattice structure.^[21] Epitaxial biaxial strain has been demonstrated to drive BFO films into tetragonal, rhombohedral, and orthorhombic structures.^[22] Recent progress in the synthesis of freestanding oxide films enables unprecedented freedom in engineering the materials' symmetry, strain, and strain gradient for novel properties.^[20,23] By taking the lateral piezoelectric force microscopy (LPFM) images with different rotation angles between the BFO films and cantilever, a polarization vector map can be extracted, showing that the polarization along the stretching direction increases under uniaxial strain (Figure 2). (More detailed information on the LPFM and data analysis can be found in the Experimental Section and the Supporting Information (Figure S7, Supporting Information).) This observation is expected, as the polarization of ferroelectric perovskites has the tendency to align with the elongated axis. For example, a phase transition from the rhombohedral "R-phase" (with polarization along a [111] direction) to the tetragonal "T-phase" (with polarization along [001]) can be driven in BFO films by the elongation of the out-of-plane *c* lattice parameter under compressive epitaxial strain.^[22] Both the clear elongation of the in-plane lattice and prominent depolarization field in thin films have the tendency to drive the polarization toward the stretching in-plane direction, which is consistent with our LPFM measurements. The polarization rotation observed here is also similar to the one recently reported for PbTiO₃.^[24]

Thermal transport properties are measured by the TDTR method based on a pump and probe technique, as schematically shown in Figure 3a. An Al metal layer is deposited on the suspended BFO film to absorb the energy from the pump beam and generate heat (the Al capping layer does not significantly affect the actual strain achieved in the BFO films under stretching, as shown in Figure S8, Supporting Information). The time-resolved reflection signal of the probe beam reflects the thermal dissipation capability, from which the thermal

transport properties of the material can be extracted. More details of our TDTR measurements are provided in the Experimental Section and the Supporting Information (Figures S10 and S11, Supporting Information). As shown in Figure 3b, the measured thermal resistance of the unstrained Al/BFO interface (obtained with ultrathin BFO films) in Al/BFO/epoxy/PEN is 0.012 m² K MW⁻¹. Remarkably, when tensile strain is applied, the thermal resistance substantially increases, up to a maximum of 0.308 m² K MW⁻¹ at 3.5% uniaxial tensile strain, which represents an enhancement of one order of magnitude. Upon a further increase of the strain, the thermal resistance decreases again, due to the relaxation of uniaxial stress and appearance of microcracks. The strain-driven variation of the thermal resistance is also reflected in the change of the slope of the fitted curves (Figure S10h, Supporting Information). This general trend and the coincident sudden change in the thermal resistance and lattice parameters (XRD measurements) of BFO imply that the thermal resistance variation is correlated with the effective strain and lattice deformation. As shown in Figure 3c, the TDTR measurement on Al/epoxy/PEN—a similar structure, but without BFO film—does not show any strain dependence of the thermal resistance (curve fitting shown in Figure S12, Supporting Information), thus implying that the giant thermal resistance change is related to the presence of BFO and rules out the possible influence caused by elastic piezoreflectance

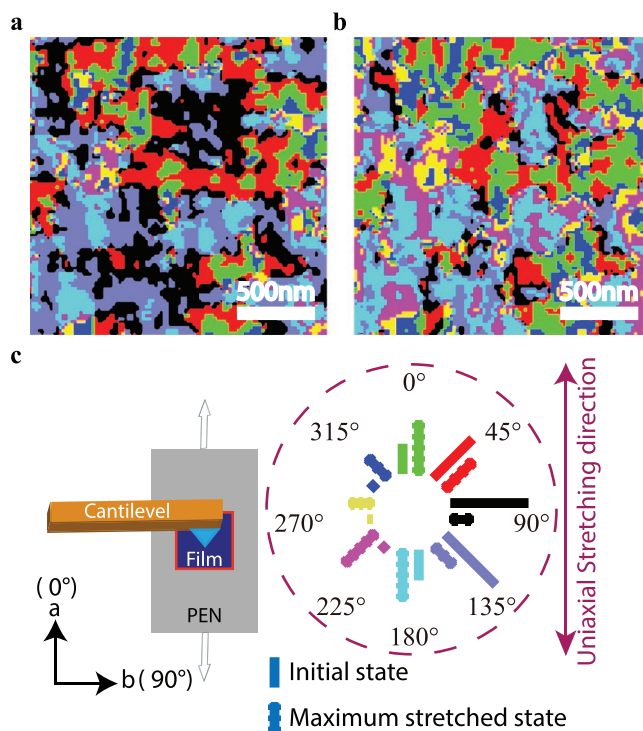


Figure 2. Evolution of the polarization in freestanding BFO films (5.2 nm) under uniaxial strain. a,b) In-plane domain structure measured by LPFM polarization vector mapping for the bare freestanding BFO film under 0% (a) and 3.5% (b) uniaxial strain. c) Evolution of the domain volume projected along different in-plane directions showing the increase of the domains with polarization along the stretching direction. The left image shows the definition of azimuth angle between cantilever and sample stretching direction, the right image represents the distributions of in-plane projected polarizations.

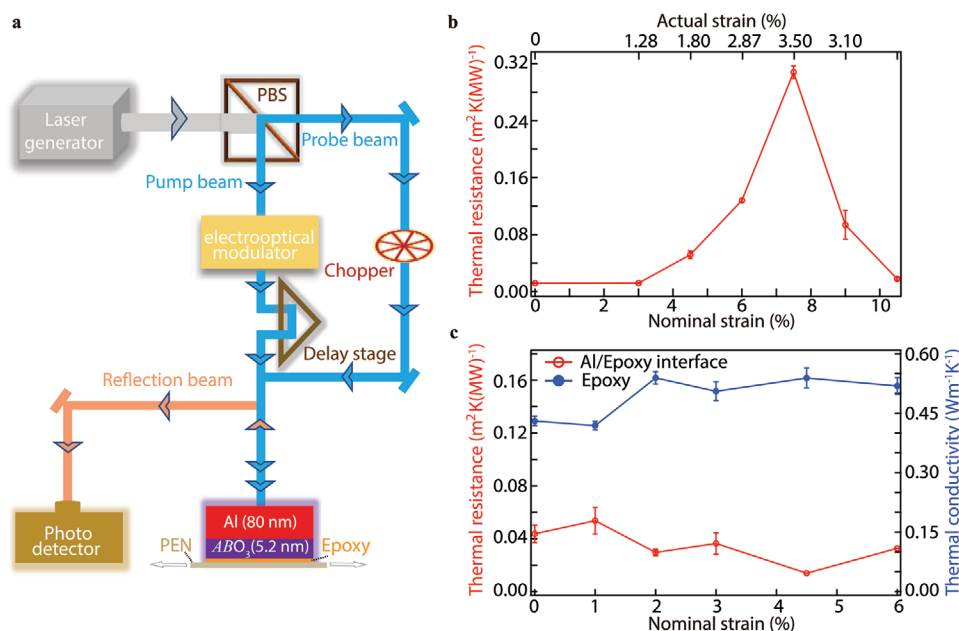


Figure 3. Thermal transport properties of Al/BFO measured by TDTR technique. a) Schematic of the TDTR technique based on a pump-and-probe technique. b) Thermal resistance of Al/BFO interface as a function of strain. It shows a drastic increase of the thermal resistance as strain increases and reaches a maximum value before the lattice starts to relax due to the formation of microcracks. c) Thermal resistance of Al/epoxy interface (red line) and thermal conductivity of epoxy (blue line) have negligible variation under strain, indicating the strain-dependent thermal resistance is related to Al/BFO interface.

effects in polymers.^[25] We have measured the interfacial thermal conductance of Al/BFO with varying Al and BFO thicknesses, showing that both the thicknesses of the Al and BFO layers do not significantly affect the interfacial thermal conductance (Figures S13 and S14, Supporting Information). Scanning electron microscopy (SEM) and energy-dispersive spectrometry (EDS) measurements have been performed and neither cracks/gaps nor chemical distribution changes have been found at the interface before and after stretching (Figure S15, Supporting Information). Moreover, we further show that the epoxy can form atomically smooth surfaces by directly gluing PEN on a SAO sacrificial layer. After dissolving the SAO layer away, the surface of the epoxy layer is exposed to air, showing an atomically smooth steps-and-terraces surface (Figure S16, Supporting Information). These results rule out the effects of interface chemical state and flatness on the interfacial thermal conductance.

We now discuss possible mechanisms underlying the giant strain-driven tunability of thermal transport in Al/BFO. There are several possible explanations: 1) The observed thermal resistance effects may be related to the variation of the domain wall density in BFO films, since domain walls are believed to scatter phonons and affect the thermal transport properties of ferroelectrics.^[12a] 2) As uniaxial strain is applied on the BFO films, the crystal structure distortion and polarization rotations may result in strong anisotropy of the thermal conductivity in BFO films. 3) The observed thermal resistance effects may be related to the Al/BFO interface because the strain-driven BFO polarization rotation alters the density of bound charges at it, which may affect the interfacial electron–phonon coupling and interface thermal resistance.

The first two mechanisms can be ruled out by experimental evidences and theoretical calculations. First, as shown in Figure 2a,b and Figure S17 in the Supporting Information, LPFM measurements show that the domain wall density only slightly increases under strain. This also agrees with our phase-field simulations, which show little differences between the domain wall density of strained and unstrained BFO (Figure S18, Supporting Information). Second, as a pseudo-cubic material, the anisotropy of the thermal conductivity of BFO itself should be small. First-principles density functional theory (DFT) calculations show, indeed, that changes in the BFO thermal conductivity, κ , induced by uniaxial strains of up to 6% are less than 2% (Figure S19, Supporting Information). The DFT calculations also reveal that, as regards thermal conductivity, the anisotropy of rhombohedral (R3c) bulk BFO is almost negligible and barely amounts to 3% (Figure S19, Supporting Information), thus a simple strain-driven rotation of the lattice cannot explain by itself the observed effect (in contrast, see ref. [26] for a strong anisotropy effect in $PbTiO_3$). Similar conclusions can be drawn if we assume that upon strain BFO becomes super-tetragonal and its anisotropy increases. The reduction in thermal conductivity resulting from such an anisotropy increase may be at most of 20%, which is again too small to explain our observations (see the Experimental Section for full details on the DFT calculations). It is worth noticing that within the same computational setup we predict a thermal conductivity for unstrained R3c BFO that is in excellent agreement with the experimental observations,^[11] which confirms the reliability of our first-principles DFT results. Furthermore, previous experimental works on the “T-phase” and “R-phase” of BFO also show small κ differences between them.^[11]

As a result, the giant tuning of the thermal conductance that we measured is most likely related to the Al/BFO (metal/ferroelectric) interface. As discussed above, the thermal energy carried by the electrons in Al must be transferred to the phonons in BFO through direct electron–phonon coupling between the metal and ferroelectric or by electron–phonon coupling in Al followed by subsequent phonon–phonon interaction across the interface. Note that there is an insulator/insulator interface (BFO/epoxy) in addition to the Al/BFO interface. Our TDTR experiments show that the impact of the polarization switching on the interfacial thermal conductivity at a ferroelectric/epoxy interface is negligible (Figure S20, Supporting Information).

For the interface between a metal and an ionic insulator, the former mechanism—i.e., direct coupling between metallic charges and phonons in the oxide—is expected to be dominant.^[27] If the ionic insulator is a ferroelectric oxide, and especially if the spontaneous polarization (or at least a component of it) is perpendicular to the metal/ferroelectric interface, this mechanism can be expected to be even more prevalent. In such a case, free charges accumulate on the metallic side of the interface to compensate (screen) the bound charge associated with the spontaneous polarization. Likewise, the natural thermal fluctuations of the polarization (which can be thought of as a strongly polar phonon pointing at the interface) effectively generates an oscillating electric field that couples to the screening charges (and, more generally, to the surface plasmons of the metal), which in turn couple to the electrons in the bulk of the metal. Then, strain (or an external electric field) can alter the distribution of polarization bound charges and metal screening near the interface, thus modifying the corresponding direct electron–phonon coupling. In particular, when the polarization rotates and lies in-plane, there is neither a permanent accumulation of free charges at the interface nor a large and oscillating polarization coupled to them; hence, we can expect a smaller coupling with the surface plasmon on the metal side. Indeed, our first-principles DFT simulations of an Al/BFO interface system provide numerical evidence for a smaller accumulation of interface screening charges in the metallic Al side when the BFO polarization is oriented parallel to the Al/BFO interface (Figure S21, Supporting Information). It follows then that the direct electron–phonon coupling becomes less efficient and consequently the thermal resistance of the interface should increase. Note that piezoelectric and pyroelectric effects should be negligible in this case. Since the strain is applied along the in-plane direction, the piezoelectric effect does not alter the surface bound charge in addition to the ferroelectric polarization rotation effect. Also, since the experiments on strained and unstrained samples were performed under identical environmental conditions and the calculated temperature change due to the laser heating is <10 K (Equation 3 from the Supporting Information in ref. [5c]), the pyroelectric effects should be negligible as well.^[28]

The above interface thermal resistance scenario is formally described within the theory developed by Mahan for metal/insulator interfaces,^[27] when the latter are polar. Therein, the thermal resistance of the interface reads as $r_i = (\sigma_0 \mathcal{I})^{-1}$, where σ_0 is a constant that depends on the properties of the two bulk materials and the system geometry, and thus in principle can be considered independent of the possible spontaneous polarization of the insulator. \mathcal{I} , on the other hand, is an integral function

that depends proportionally on the ionic charges near the interface and inversely on the dielectric constant of the insulator. Ferroelectrics are characterized by very large ionic (bound) charges associated with their spontaneous polar distortion; hence, if the ferroelectric polarization points toward the interface, this will contribute to a large value of \mathcal{I} and, thus, yield a small thermal resistance (Figure 4c). Note also that our first-principles DFT calculations indicate that the anisotropy of the dielectric constant (and thus of the screening) is not substantial in BFO. Hence, \mathcal{I} is essentially controlled by the orientation of the polarization with respect to the metal/ferroelectric interface. In particular, rotation of the polarization away from the interface should result in reduced interfacial bound charges, thus a reduced \mathcal{I} and an increased thermal resistance, exactly as observed. In contrast to the typical 180° switching of ferroelectric polarizations, the synthesis of high-quality freestanding films and the giant strain tunability in these materials allow the in situ polarization switching from out-of-plane to in-plane directions and thus enable the intriguing observations reported in this work.

To further confirm the fact that interfacial thermal transport can be tuned by changing the orientation of the ferroelectric polarization, we performed TDTR experiments on other metal/ferroelectric interfaces, namely, Al/LiNbO₃ and Al/BaTiO₃, where LiNbO₃ (LNO) and BaTiO₃ (BTO) are single crystals in a nearly ferroelectric monodomain state. Interfaces with various polarization orientations are explored by depositing the Al film on different surfaces of the crystals, always maintaining the same surface smoothness and quality (Figure 4a,b). As shown in Figure 4a, when the polarization is lying in-plane, the interface thermal resistance of Al/LNO is increased by nearly a factor of 3 as compared to the case with perpendicular upward polarization, which is consistent with the trend observed for the Al/BFO interface. As expected, the size of the interface thermal resistance increase is smaller in this case because the experiments were performed for a bulk crystal rather than for ultrathin membranes, and thus the relative weight of the interface contribution to the overall thermal resistance is lower. Interestingly, the interface thermal resistance corresponding to the polarization pointing toward the interface is lower than that for the polarization pointing away from the interface, in agreement with our results obtained in ultrathin membranes. Similar to that case, a higher density of free electrons is accumulated at the interface when the polarization is pointing toward the interface. Since it is very difficult to prepare ideal monodomain BTO crystals, our BTO crystal presents mixed in-plane and out-of-plane polarizations (Figure S22, Supporting Information). Nonetheless, the polarization along the out-of-plane direction is a single phase, thus allowing for the comparison of the interface thermal resistance between the upward and downward polarization configurations (Figure 4b): the results actually coincide with those obtained for the Al/LNO interface. Data fitting and ratio sensitivity of TDTR measurement for LNO and BTO are shown in Figure S23 in the Supporting Information.

3. Conclusion

We have reported the observation of an unusually large modulation of the thermal transport across metal/ferroelectric

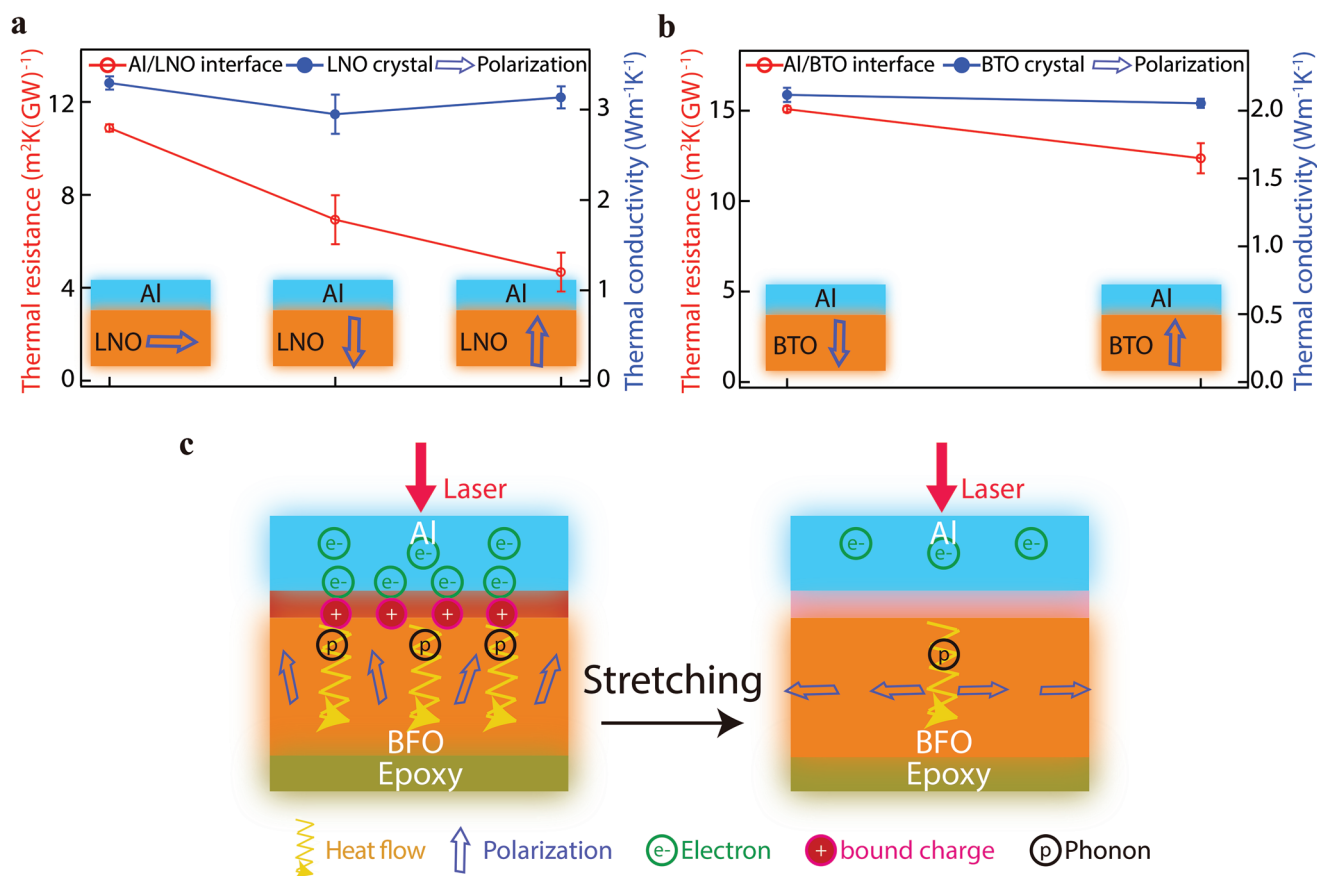


Figure 4. Strong dependence of the thermal resistance on the ferroelectric polarization orientation. a) Thermal resistance of Al/LiNbO₃ (LNO) interface (red line) and thermal conductivity of LNO crystal (blue line) measured by TDTR on LNO crystals with different polarization orientations, showing the highest (lowest) thermal resistance at the interface with in-plane (upward) polarization. b) Thermal resistance of Al/BaTiO₃ (BTO) interface (red line) and thermal conductivity of BTO crystal (blue line) measured by TDTR on BTO crystals with different polarization orientations, showing higher (lower) thermal resistance at the interface with downward (upward) polarization. c) Schematic cartoon depicting the mechanisms of the giant regulation of thermal transport by controlling the polarization orientation, and thus the density of bound charges and free electrons at the interface, by applying uniaxial strain.

interfaces by applying uniaxial strain to engineer the polarization orientation in the ferroelectric layer. Our results reveal that interface bound charges have a drastic effect on the electron–phonon-mediated thermal coupling between the metal and the insulator layers. Electron–phonon interactions have been shown to alter bulk phonon heat transport,^[29] but here we report an unprecedented and, most importantly, dynamically tunable heat resistance interface effect. This exceptionally large strain–thermal effect is of great interest for fundamental investigations and technological applications, as it demonstrates selective opening of an interface heat dissipation channel by rotating the polarization. Note that the ferroelectric polarization can be effectively rotated by external electric fields as well. In real applications in electronics, depositing a thin layer of ferroelectric materials between metal/insulator interfaces and applying an electric field to orient the polarization pointing to the metal layer, could effectively lower the interface thermal resistance. Our work thus provides a new mechanism to optimize the thermal management of next-generation nanodevices, power electronics, and thermal logic devices.

4. Experimental Section

Epitaxial Film Growth, Transfer, and Structure Characterizations: The multiferroic BFO and water-soluble sacrificial SAO films were prepared by oxide molecular beam epitaxy (OMBE). First, (001) oriented SAO films were deposited on a (001) oriented STO substrate at 850 °C with O₂ partial pressure of 1.29E-9 torr, then the BFO films were grown on SAO at 380 °C in ozone atmosphere with a partial pressure of ozone of 3.5E-8 torr. The quality of films was monitored by reflection high-energy electron diffraction (RHEED; Figure S1d, Supporting Information). The detailed description of film preparation is described in a previous report.^[19b]

In order to apply uniaxial strain, the BFO film was transferred to the flexible substrate PEN. Epoxy adhesive was applied in order to improve the bonding force between the film and PEN. The specific film transfer process is shown in Figure 1a: First, a thin layer of epoxy was applied on the BFO film and then the PEN was attached on the top surface of the epoxy. Next, the sample was heated at 100 °C for 0.5 h to cure the epoxy. Then, the cured sample was dipped into water to dissolve the SAO film, which typically took 2 days. When the SAO film was completely dissolved, the substrate was removed easily, leaving the final BFO/epoxy/PEN sample for measurements. Uniaxial strain was applied on the PEN using a homemade stretching setup. The flexible substrate PEN was fixed on the linear stages and the tensile force was exerted along two opposing directions (Figure S4, Supporting Information). The strain generated by

the stretched PEN was transferred to the film through the epoxy. The nominal strain was defined as the percentage of the elongation of PEN substrate, and the actual strain was defined as the percentage of the real lattice expansion measured by in situ XRD (Figure 1b). As shown in Figures S1–S3 and S5 in the Supporting Information, the quality of the film and evolution of the lattice parameters under strain were measured by XRD, X-ray reflection (XRR), and reciprocal-space mapping (RSM), which was operated on a Bruker D8 Discover X-ray diffractometer.

Piezoresponse Force Microscopy Measurements and Data Processing: The topography and ferroelectric properties of strained BFO films on a flexible PEN were measured by Asylum Research MFP-3D Origin+. In order to apply an electric field effectively, a conductive carbon layer was coated on the backside of the PEN. Considering both the amplitude and phase data of a specific position at different sample rotation angles, a series of projection (signed values) varied with sample rotation angles was derived, which was fitted well by a sine function. Thus, the polarization state of each point in the overlapping area was determined by the polarization and phase shift of the fitting curve.^[30] Then 360° was divided into eight directions uniformly (each one occupied 45°, according to the polarization of BFO) and the in-plane polarization direction was classified. The polarizations were represented by different colors, the final treated polarization diagrams are shown in Figure 2c.

TDTR Measurements: Thermal dissipation capacity of the freestanding BFO films was characterized by the TDTR method. TDTR was a method suitable for measuring thermal properties of thin-film materials and the fundamental principle of the method is described elsewhere.^[13] Mechanism explanation of TDTR measurement is shown in Figure 3a. Ti:sapphire (Chameleon, Coherent) generated femtosecond laser pulses with central wavelength around 800 nm. The incoming laser was divided into a pump beam and a probe beam by a polarizing beam splitter. The amplitude of the pump beam was modified as radio frequency sine wave, and the intensity of the probe beam was modified by a chopper. Then the path of the pump beam was tuned continuously by the delay stage, which allowed delays with 0–4 ns. The pump beam was irradiated on the surface of the sample, generating the heat, and the heat was transferred down into the sample. The surface temperature of the material was related to its thermal conductivity, which affected the reflection efficiency of the probe beam. Thus, the thermal conductivity of the material could be obtained from the reflection signal of the probe beam. The pump beam was modulated at 9.8 MHz and the probe beam was chopped at 180 Hz to improve the signal-to-noise ratio. The powers were 23 and 12 mW for the pump and probe, respectively. Since there was no difference between the measurements performed in air or under vacuum (Figure S9, Supporting Information), all the TDTR data were taken in open air at room temperature. Based on the total laser beam power (35 mW), the laser spot size (radius = 12 μm) on the sample surface, and the absorption rate (0.15) of the transducer layer, the incident thermal power density was calculated as $1.16 \times 10^7 \text{ W m}^{-2}$ in this case. In this work, the freestanding BFO films were supported by epoxy and an ≈80 nm Al film was deposited onto the samples by magnetron sputtering to serve as heat transducer. The Al and BFO in-plane dimensions were $2.5 \times 2.5 \text{ mm}^2$. Note that since thicker films were brittle and easy to form cracks before the phase transition (Figure S6, Supporting Information), a thin BFO film (5.2 nm by XRR in Figure S2, Supporting Information) was used in this work. Following the method used in the literature,^[31] for a reliable data fitting, the BFO film was treated as part of the interface, while bulk thermal conductivity of Al and epoxy were included in the data fitting. All the fitting parameters, volumetric specific heat of Al, BFO, BTO, LNO, and epoxy are obtained from the homepage of the group of David. G. Cahill (<https://cahill.matse.illinois.edu/software-and-data>) or from the literature as shown in Table S1 in the Supporting Information.^[32] The thermal resistance of BFO films and thermal conductivity of epoxy were fitting parameters in the processing of data.

SEM/EDS Measurements: SEM/EDS characterization was operated on a Zeiss Ultra 55 with extra high tension of 10 kV, the vacuum state was nearly 7.17×10^{-7} mbar. For cross-sectional samples preparation, the upper and lower surfaces of Al/BFO/epoxy/PEN were adhered to silicon wafers by glue to maintain the strain state. The cured samples were cut

along the cross-section plane with a saw and the exposed cross-section plane was polished with diamond lapping papers (the minimum particle size was 0.1 μm) to improve the surface flatness.

Phase Field Simulations: The phase-field method was employed to study the strain effect on the domain structures and the corresponding effective thermal conductivity. In the phase-field model of ferroelectric thin film, the polarization field **P** was selected as the order parameter to describe the domain structures.^[33]

The spatial and temporal evolution of the polarization under external thermal, electric, and mechanical stimuli was controlled by the time-dependent Ginzburg–Landau (TDGL) equation

$$\frac{\partial \mathbf{P}(\mathbf{x}, t)}{\partial t} = -L \frac{\delta F}{\delta \mathbf{P}(\mathbf{x}, t)} \quad (1)$$

where L represents the kinetic coefficient related to the domain wall mobility. The total free energy in Equation (1) includes contributions from the bulk chemical energy (f_{bulk}), polarization gradient energy (f_{grad}), electric energy (f_{electric}), and elastic energy (f_{elastic}), i.e.,

$$F = \iiint_V [f_{\text{bulk}}(\mathbf{P}, T) + f_{\text{grad}}(\nabla \mathbf{P}) + f_{\text{electric}}(\mathbf{P}, \mathbf{E}) + f_{\text{elastic}}(\mathbf{P}, \boldsymbol{\varepsilon})] dV \quad (2)$$

where $\boldsymbol{\varepsilon}$, **E**, $\nabla \mathbf{P}$ represent the strain tensor, electric field vector, and polarization gradient, respectively. One could also include other contributions such as chemical potentials of charged defects and flexoelectric coupling in Equation (2). The expressions of each energy term can be found in previous review papers.^[33] The electric-field and stress distributions coupled with the domain structures were determined by solving the electrostatic equilibrium equation with short-circuit electric boundary conditions and elastic equilibrium equation with strained boundary conditions, respectively. A system size of $200\Delta x \times 200\Delta x \times (N_{\text{Substrate}} + N_{\text{BFO}} + N_{\text{Air}})\Delta z$ with $\Delta x = \Delta z = 1 \text{ nm}$, $N_{\text{Substrate}} = 12$, $N_{\text{BFO}} = 10$, and $N_{\text{Air}} = 4$ was employed to do the phase-field simulations of domain structures. Material parameters of BFO used in the simulation were taken from the literature.^[34] To calculate the effective thermal conductivity of different domain structures, the heat conduction equation was solved

$$\frac{\partial}{\partial x_i} \left(k_{ij}(\mathbf{x}) \frac{\partial T(\mathbf{x})}{\partial x_j} \right) + q(\mathbf{x}) = \rho c_p \frac{\partial T(\mathbf{x})}{\partial t} \quad (3)$$

where $k_{ij}(\mathbf{x})$ is the spatial-dependent thermal conductivity tensor, $T(\mathbf{x})$ is the temperature distribution, ρ , c_p , and $q(\mathbf{x})$ are the mass density, specific heat capacity, and the internal heat source of the material, respectively. The spatially dependent thermal conductivity in a ferroelectric thin film with domain structure then was described as follows^[35]

$$k_{ij}(\mathbf{x}) = k_{ij}^{\text{fs-wall}} \eta(\mathbf{x}) + k_{ij}^{\text{domain}} (1 - \eta(\mathbf{x})) \quad (4)$$

where $k_{ij}^{\text{fs-wall}}$ and k_{ij}^{domain} represent the individual thermal conductivity of the ferroelastic domain wall and domain, respectively. In the simulation, the domain and domain wall thermal conductivities of 1.0 and 0.1 $\text{W m}^{-1} \text{ K}^{-1}$, respectively, were assumed arising from their different phonon scattering abilities observed in experiments.^[12a, 12b] The heat conduction equation was solved using a spectral iterative perturbation method, which can be found in the literature.^[35]

First-Principles Calculations of the Thermal Conductivity of BFO: The second- and third-order interatomic force constants (IFCs) were computed within DFT as implemented in the VASP code,^[36] using the local density approximation for the exchange-correlation energy functional and a plane-wave cutoff of 500 eV with the projector augmented-wave method.^[37] The IFCs were calculated from finite differences and the inequivalent displacements were generated with the PHONOPY^[38] and THIRDDORDER.PY^[39] codes. A $3 \times 3 \times 3$ and a $2 \times 2 \times 2$ supercell of the rhombohedral primitive cell were used for the second- and third-order IFCs, respectively.

In the case of an applied strain of 6%, the experimental lattice parameters were considered. It was started with a 40-atom cell where

it was easy to impose the pseudo-cubic lattice parameters. With this distortion of the cell and a full optimization of atomic positions and cell angles, a structure was obtained that, provided that deviations of 0.1 Å were accepted, had a Cc symmetry, which corresponds to a 20-atom unit cell. For this unit cell, both the second- and third-order IFCs were computed in a $2 \times 2 \times 2$ supercell.

The computed IFCs were used as inputs to solve the linearized phonon Boltzmann transport equation (BTE) using the iterative method implemented in the SHENGBTE code.^[39] The lattice thermal conductivity was obtained as

$$\kappa^{\alpha\beta} = \frac{1}{k_B T^2 V N} \sum_{\lambda} f_0(f_0 + 1) (\hbar \omega_{\lambda})^2 v_{\lambda}^{\alpha} F_{\lambda}^{\beta} \quad (5)$$

where α and β are the three coordinate directions x , y , and z ; and k_B , T , V , and N are the Boltzmann constant, the temperature, the volume of the unit cell, and the number of \mathbf{q} points, respectively. The sum runs over all the phonon modes λ , which have wave-vector \mathbf{q} and branch v . f_0 is the equilibrium Bose–Einstein distribution function, \hbar is the reduced Planck constant, and ω_{λ} and v_{λ}^{α} are the phonon frequency and phonon group velocity. F_{λ}^{β} is initially taken to be equal to $\tau_{\lambda} v_{\lambda}^{\beta}$, where τ_{λ} is the lifetime of the phonon mode λ within the relaxation time approximation (RTA). The BTE was solved on a $10 \times 10 \times 10$ and a $3 \times 5 \times 4$ grid of \mathbf{q} -points for the unstrained R3c and strained Cc case, respectively.

Additionally, an Al/BFO interface system was simulated in which the electric polarization of the BFO layer was forced to be oriented along: 1) the pseudo-cubic [110] direction, which was parallel to the Al/BFO interface, and 2) the pseudo-cubic [111] direction, which was not parallel to the Al/BFO interface (Figure S21, Supporting Information). The Al region contained a total of 72 atoms and was ≈ 18 Å thick, while the BFO region contained a total of 152 atoms and was ≈ 27 Å thick. The fcc lattice parameters and atomic positions in the Al region were adjusted to minimize the strain at the Al/BFO interface, while the lattice parameters and atomic positions in the BFO region were kept fixed in order to constrain the direction and size of the corresponding polarization. Periodic boundary conditions were applied along the three lattice vectors defining the simulation supercell. Planar and macroscopic average potentials were then estimated along the direction perpendicular to the Al/BFO interface for systems (1) and (2) in order to quantify the magnitude of the dipole moment created at the Al/BFO interface, which could be ascribed to the presence of bound charges in the ferroelectric BFO side and of free screening charges in the metallic Al side. Macroscopic average potentials were obtained by taking averages of the planar potential over distances of one unit cell along the same direction.

Supporting Information

Supporting Information is available from the Wiley Online Library or from the author.

Acknowledgements

Y.Z., C.D., and Z.G. contributed equally to this work. This work was supported by the National Natural Science Foundation of China (nos. 11774153, 51772143, 11474158, 11890700, 11904162, 1861161004, 11625418, 11974163, 51732006, 52027803, 61704074, and 91963211), the National Basic Research (Key R&D) Program of China (2017YFA0303702 and 2018YFA0306200), the introduced innovative R&D team of Guangdong (2017ZT07C062), the Foundation for Innovative Research Groups of the National Natural Science Foundation of China (51720001), and the Fundamental Research Funds for the Central Universities (nos. 0213-14380198 and 0213-14380167). Y.N. was supported by High-Level Entrepreneurial and Innovative Talents Introduction, Jiangsu Province. Theoretical work was funded by the Luxembourg National Research Fund

through project FNR/C18/MS/12705883/REFOX. (H.A. and J.Í.). C.C. acknowledges support from the Spanish Ministry of Science, Innovation, and Universities under the “Ramón y Cajal” fellowship RYC2018-024947-I. R.R. acknowledges financial support by the Ministerio de Ciencia e Innovación (MICINN) under grant FEDER-MAT2017-90024-P and the Severo Ochoa Centres of Excellence Program under Grant CEX2019-000917-S and by the Generalitat de Catalunya under grants no. 2017 SGR 1506. The authors thank the Centro de Supercomputación de Galicia (CESGA) for the use of their computational resources. The authors thank Yaya Zhou for the support of SEM and EDS measurement.

Conflict of Interest

The authors declare no conflict of interest.

Data Availability Statement

The data that support the findings of this study are available from the corresponding author upon reasonable request.

Keywords

electron–phonon coupling, freestanding films, metal/ferroelectric interfaces, thermal resistance tuning, uniaxial strain

Received: July 26, 2021

Revised: October 13, 2021

Published online:

- [1] a) P. Ball, *Nature* **2012**, 492, 174; b) S. Li, Q. Y. Zheng, Y. C. Lv, X. Y. Liu, X. Q. Wang, P. S. E. Y. Huang, D. G. Cahill, B. Lv, *Science* **2018**, 361, 579.
- [2] a) L. J. Cui, S. Hur, Z. A. Akbar, J. C. Klockner, W. Jeong, F. Pauly, S. Y. Jang, P. Reddy, E. Meyhofer, *Nature* **2019**, 572, 628; b) N. Mosso, U. Drechsler, F. Menges, P. Nirmalraj, S. Karg, H. Riel, B. Gotsmann, *Nat. Nanotechnol.* **2017**, 12, 430; c) J. Y. Wang, L. Y. Zhu, J. Chen, B. W. Li, J. T. L. Thong, *Adv. Mater.* **2013**, 25, 6884.
- [3] S. S. Chen, Q. Z. Wu, C. Mishra, J. Y. Kang, H. J. Zhang, K. J. Cho, W. W. Cai, A. A. Balandin, R. S. Ruoff, *Nat. Mater.* **2012**, 11, 203.
- [4] a) S. Vaziri, E. Yalon, M. M. Rojo, S. V. Suryavanshi, H. R. Zhang, C. J. McClellan, C. S. Bailey, K. K. H. Smithe, A. J. Gabourie, V. Chen, S. Deshmukh, L. Bendersky, A. V. Davydov, E. Pop, *Sci. Adv.* **2019**, 5, eaax1325; b) Z. W. Chen, X. Y. Zhang, Y. Z. Pei, *Adv. Mater.* **2018**, 30, 1705617.
- [5] a) M. N. Luckyanova, J. Garg, K. Esfarjani, A. Jandl, M. T. Bulsara, A. J. Schmidt, A. J. Minnich, S. Chen, M. S. Dresselhaus, Z. F. Ren, E. A. Fitzgerald, G. Chen, *Science* **2012**, 338, 936; b) R. Cheaito, J. C. Duda, T. E. Beechem, K. Hattar, J. F. Ihlefeld, D. L. Medlin, M. A. Rodriguez, M. J. Campion, E. S. Piekos, P. E. Hopkins, *Phys. Rev. Lett.* **2012**, 109, 195901; c) J. Ravichandran, A. K. Yadav, R. Cheaito, P. B. Rossen, A. Soukiasian, S. J. Suresha, J. C. Duda, B. M. Foley, C. H. Lee, Y. Zhu, A. W. Lichtenberger, J. E. Moore, D. A. Muller, D. G. Schlom, P. E. Hopkins, A. Majumdar, R. Ramesh, M. A. Zurbuchen, *Nat. Mater.* **2014**, 13, 168; d) M. Maldovan, *Nat. Mater.* **2015**, 14, 667.
- [6] I. Zardo, R. Rurali, *Curr. Opin. Green Sustain. Chem.* **2019**, 17, 1.
- [7] a) A. Giri, P. E. Hopkins, *Adv. Funct. Mater.* **2020**, 30, 1903857; b) G. Hamaoui, N. Horny, Z. L. Hua, T. Q. Zhu, J. F. Robillard, A. Fleming, H. Ban, M. Chirtoc, *Sci. Rep.* **2018**, 8, 11352.

- [8] A. Majumdar, P. Reddy, *Appl. Phys. Lett.* **2004**, *84*, 4768.
- [9] E. T. Swartz, R. O. Pohl, *Rev. Mod. Phys.* **1989**, *61*, 605.
- [10] a) J. Cho, M. D. Losego, H. G. Zhang, H. Kim, J. M. Zuo, I. Petrov, D. G. Cahill, P. V. Braun, *Nat. Commun.* **2014**, *5*, 4035; b) Y. F. Tsai, P. C. Wei, L. W. Chang, K. K. Wang, C. C. Yang, Y. C. Lai, C. R. Hsing, C. M. Wei, J. He, G. J. Snyder, H. J. Wu, *Adv. Mater.* **2021**, *33*, 2005612; c) T. Xing, C. X. Zhu, Q. F. Song, H. Huang, J. Xiao, D. D. Ren, M. J. Shi, P. F. Qiu, X. Shi, F. F. Xu, L. D. Chen, *Adv. Mater.* **2021**, *33*, 2008773.
- [11] S. Ning, S. C. Huberman, C. Zhang, Z. J. Zhang, G. Chen, C. A. Ross, *Phys. Rev. Appl.* **2017**, *8*, 054049.
- [12] a) E. Langenberg, D. Saha, M. E. Holtz, J. J. Wang, D. Bugallo, E. Ferreira-Vila, H. Paik, I. Hanke, S. Ganschow, D. A. Muller, L. Q. Chen, G. Catalan, N. Domingo, J. Malen, D. G. Schlom, F. Rivadulla, *Nano Lett.* **2019**, *19*, 7901; b) P. E. Hopkins, C. Adamo, L. H. Ye, B. D. Huey, S. R. Lee, D. G. Schlom, J. F. Ihlefeld, *Appl. Phys. Lett.* **2013**, *102*, 121903; c) A. J. H. Mante, J. Volger, *Physica* **1971**, *52*, 577; d) M. A. Weilert, M. E. Msall, A. C. Anderson, J. P. Wolfe, *Phys. Rev. Lett.* **1993**, *71*, 735; e) J. F. Ihlefeld, B. M. Foley, D. A. Scrymgeour, J. R. Michael, B. B. McKenzie, D. L. Medlin, M. Wallace, S. Trolier-McKinstry, P. E. Hopkins, *Nano Lett.* **2015**, *15*, 1791; f) B. M. Foley, M. Wallace, J. T. Gaskins, E. A. Paisley, R. L. Johnson-Wilke, J. W. Kim, P. J. Ryan, S. Trolier-McKinstry, P. E. Hopkins, J. F. Ihlefeld, *ACS Appl. Mater. Interfaces* **2018**, *10*, 25493.
- [13] M. D. Losego, M. E. Grady, N. R. Sottos, D. G. Cahill, P. V. Braun, *Nat. Mater.* **2012**, *11*, 502.
- [14] P. E. Hopkins, L. M. Phinney, J. R. Serrano, T. E. Beechem, *Phys. Rev. B* **2010**, *82*, 085307.
- [15] T. S. English, J. C. Duda, J. L. Smoyer, D. A. Jordan, P. M. Norris, L. V. Zhigilei, *Phys. Rev. B* **2012**, *85*, 035438.
- [16] M. Dawber, K. M. Rabe, J. F. Scott, *Rev. Mod. Phys.* **2005**, *77*, 1083.
- [17] J. F. Scott, *Science* **2007**, *315*, 954.
- [18] a) E. Y. Tsybal, H. Kohlstedt, *Science* **2006**, *313*, 181; b) V. Garcia, S. Fusil, K. Bouzehouane, S. Enouz-Vedrenne, N. D. Mathur, A. Barthelemy, M. Bibes, *Nature* **2009**, *460*, 81.
- [19] a) D. Lu, D. J. Baek, S. S. Hong, L. F. Kourkoutis, Y. Hikita, H. Y. Hwang, *Nat. Mater.* **2016**, *15*, 1255; b) D. Ji, S. Cai, T. R. Paudel, H. Sun, C. Zhang, L. Han, Y. Wei, Y. Zang, M. Gu, Y. Zhang, W. Gao, H. Huyan, W. Guo, D. Wu, Z. Gu, E. Y. Tsybal, P. Wang, Y. Nie, X. Pan, *Nature* **2019**, *570*, 87; c) R. J. Xu, J. W. Huang, E. S. Barnard, S. S. Hong, P. Singh, E. K. Wong, T. Jansen, V. Harbola, J. Xiao, B. Y. Wang, S. Crossley, D. Lu, S. Liu, H. Y. Hwang, *Nat. Commun.* **2020**, *11*, 3141.
- [20] L. Han, Y. H. Fang, Y. Q. Zhao, Y. P. Zang, Z. B. Gu, Y. F. Nie, X. Q. Pan, *Adv. Mater. Interfaces* **2020**, *7*, 1901604.
- [21] H. W. Jang, S. H. Baek, D. Ortiz, C. M. Folkman, R. R. Das, Y. H. Chu, P. Shafer, J. X. Zhang, S. Choudhury, V. Vaithyanathan, Y. B. Chen, D. A. Felker, M. D. Biegalski, M. S. Rzchowski, X. Q. Pan, D. G. Schlom, L. Q. Chen, R. Ramesh, C. B. Eom, *Phys. Rev. Lett.* **2008**, *101*, 107602.
- [22] D. Sando, A. Barthelemy, M. Bibes, *J. Phys. Condens. Matter* **2014**, *26*, 473201.
- [23] a) S. S. Hong, M. Gu, M. Verma, V. Harbola, B. Y. Wang, D. Lu, A. Vailionis, Y. Hikita, R. Pentcheva, J. M. Rondinelli, H. Y. Hwang, *Science* **2020**, *368*, 71; b) G. H. Dong, S. Z. Li, M. T. Yao, Z. Y. Zhou, Y. Q. Zhang, X. Han, Z. L. Luo, J. X. Yao, B. Peng, Z. Q. Hu, H. B. Huang, T. T. Jia, J. Y. Li, W. Ren, Z. G. Ye, X. D. Ding, J. Sun, C. W. Nan, L. Q. Chen, J. Li, M. Liu, *Science* **2019**, *366*, 475.
- [24] P. Torres, J. Iniguez, R. Rurali, *Phys. Rev. Lett.* **2019**, *123*, 185901.
- [25] X. J. Wang, V. Ho, R. A. Segalman, D. G. Cahill, *Macromolecules* **2013**, *46*, 4937.
- [26] J. A. Seijas-Bellido, J. Iniguez, R. Rurali, *Appl. Phys. Lett.* **2019**, *115*, 192903.
- [27] G. D. Mahan, *Phys. Rev. B* **2009**, *79*, 075408.
- [28] a) Y. B. Yao, T. Tao, B. Liang, C. L. Mak, S. G. Lu, *Ceram. Int.* **2019**, *45*, 1308; b) L. Zhang, Y. L. Huang, G. Velarde, A. Ghosh, S. Pandya, D. Garcia, R. Ramesh, L. W. Martin, *APL Mater.* **2019**, *7*, 111111.
- [29] J. Zhou, H. D. Shin, K. Chen, B. Song, R. A. Duncan, Q. Xu, A. A. Maznev, K. A. Nelson, G. Chen, *Nat. Commun.* **2020**, *11*, 6040.
- [30] J. Kim, M. You, K. E. Kim, K. Chu, C. H. Yang, *npj Quantum Mater.* **2019**, *4*, 29.
- [31] E. A. Scott, S. W. Smith, M. D. Henry, C. M. Rost, A. Giri, J. T. Gaskins, S. S. Fields, S. T. Jaszewski, J. F. Ihlefeld, P. E. Hopkins, *Appl. Phys. Lett.* **2018**, *113*, 192901.
- [32] a) Y. Wang, J. E. Saal, P. P. Wu, J. J. Wang, S. L. Shang, Z. K. Liu, L. Q. Chen, *Acta Mater.* **2011**, *59*, 4229; b) B. A. Strukov, S. T. Davitadze, S. N. Kravchun, S. A. Taraskin, M. Goltzman, V. V. Lemanov, S. G. Shulman, *J. Phys. Condens. Matter* **2003**, *15*, 4331; c) F. Lin, G. S. Bhatia, J. D. Ford, *J. Appl. Polym. Sci.* **1993**, *49*, 1901; d) S. H. Yao, J. Y. Wang, H. Liu, X. B. Hu, H. J. Zhang, X. F. Cheng, Z. C. Ling, *J. Alloys Compd.* **2008**, *455*, 501.
- [33] J. J. Wang, B. Wang, L. Q. Chen, *Annu. Rev. Mater. Res.* **2019**, *49*, 127.
- [34] J. X. Zhang, D. G. Schlom, L. Q. Chen, C. B. Eom, *Appl. Phys. Lett.* **2009**, *95*, 122904.
- [35] J. J. Wang, Y. Wang, J. F. Ihlefeld, P. E. Hopkins, L. Q. Chen, *Acta Mater.* **2016**, *111*, 220.
- [36] G. Kresse, J. Furthmuller, *Phys. Rev. B* **1996**, *54*, 11169.
- [37] P. E. Blochl, *Phys. Rev. B* **1994**, *50*, 17953.
- [38] A. Togo, I. Tanaka, *Scr. Mater.* **2015**, *108*, 1.
- [39] W. Li, J. Carrete, N. A. Katcho, N. Mingo, *Comput. Phys. Commun.* **2014**, *185*, 1747.